ACS APPLIED MATERIALS & INTERFACES

Letter

Cite This: ACS Appl. Mater. Interfaces 2019, 11, 5661−5667

www.acsami.org

Ultrasmall (<2 nm) Au@Pt Nanostructures: Tuning the Surface Electronic States for Electrocatalysis

Lucas D. Germano,[†] Valeria S. Marangoni,[†] Naga V. V. Mogili,[‡] Leandro Seixas,*[,†] and Camila M. Maroneze*[,†]

[†]MackGraphe - Graphene and Nanomaterials Research Center, Mackenzie Presbyterian University, Rua da Consolação 896, São Paulo, 01302-907, SP, Brazil

[‡]CNPEM, LNNano, Campinas, São Paulo 13083-970, Brazil

Supporting Information

ABSTRACT: The ability to tune the electronic properties of nanomaterials has played a major role in the development of sustainable energy technologies. Metallic nanocatalysts are at the forefront of these advances. Their unique properties become even more interesting when we can control the distribution of the electronic states in the nanostructure. Here, we provide a comprehensive evaluation of the electronic surface states in ultrasmall metallic nanostructures by combining experimental and theoretical methods. The developed strategy allows the controlled synthesis of bimetallic nanostructures in the core−shell configuration, dispensing of the use of any surfactant or stabilizing agents, which usually inactivate important surface phenomena. The synthesized ultrasmall Au@Pt nanoarchitecture (∼1.8 nm) presents an enhanced performance catalyzing the hydrogen evolution reaction. First-principles calculations of projected and space-resolved local density of states of $Au_{55}@Pt_{92}$ (core−shell), $Au_{55}Pt_{92}$ (alloy), and Pt_{147} nanoparticles show a prominent increase in the surface electronic states for the core−shell bimetallic nanomaterial. It arises from a more-effective charge transfer from gold to the surface platinum atoms in the core−shell configuration. In pure Pt_{147} or $Au_{55}Pt_{92}$ alloy nanoparticles, a great part of the electronic states near the Fermi level is buried in the core atoms, disabling these states for catalytic applications. The proposed experimental−theoretical approach may be useful for the design of other systems composed of metallic nanoparticles supported on distinct substrates, such as two-dimensional materials and porous matrices. These nanomaterials find several applications not only in heterogeneous catalysis but also in sensing and optoelectronic devices.

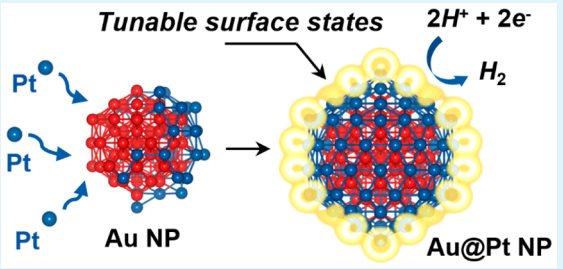

KEYWORDS: *ultrasmall nanoparticles, Au@Pt, core−shell, surface electronic states, density functional theory, electrocatalysis, hydrogen evolution reaction*

One of the major challenges in the energy field for affordable sustainable technologies is the development of efficient catalysts,[1−3] irrespective of whether the energy conversion takes place, e.g., in photovoltaic cells, in electrochemical devices or in the production of fuels from renewable sources. Among the most-studied catalytic systems, the metallic nanostructures[1] have shown remarkable properties and improved performance in essentially all the cases cited previously. Recently, the bimetallic systems and, more specifically, the core−shell architectures[4−6] have attracted huge attention. This structural design can result in significant alterations on the surface electronic states, mainly due to the charge transfer between the dissimilar metals through *d*-state hybridization[7,8] (ligand effect) and the core-induced strain on the shell layer.[9,10]

The foremost synthetic route for the synthesis of metallic core−shell architectures is the seed-mediated growth,[11,12] in which preformed nanocrystals (seeds) act as the sites for the heterogeneous nucleation of the metal atoms that build up the shell. This methodology has been successfully applied for the synthesis of a huge variety of core−shell nanostructures with sizes in the range of 5−50 nm.[6] Comparatively, much less explored are the ultrasmall nanostructures[13] (1−3 nm), which bridge the gap between molecular dispersions and larger-sized nanomaterials. At the ultrasmall size regime, the nanostructures exhibit unique properties due to the distinguished electronic states and an even-higher surface-to-volume ratio when compared with larger nanoparticles. As the size of a material decreases to 1−3 nm, most of the atoms are located on the surface, which is extremely important for catalytic applications. However, along with these advantages, the challenges regarding the atomic ordering, shape control, and stabilization of such energetically unstable structures (having high surface energies) during and after the synthesis become even more complex for multimetallic systems. The use of proper capping agents is practically indispensable, although it commonly leads to the passivation or inactivation of catalytic sites on the

Received: July 26, 2018
Accepted: January 29, 2019
Published: January 29, 2019

DOI: 10.1021/acsami.8b12712
ACS Appl. Mater. Interfaces 2019, 11, 5661−5667

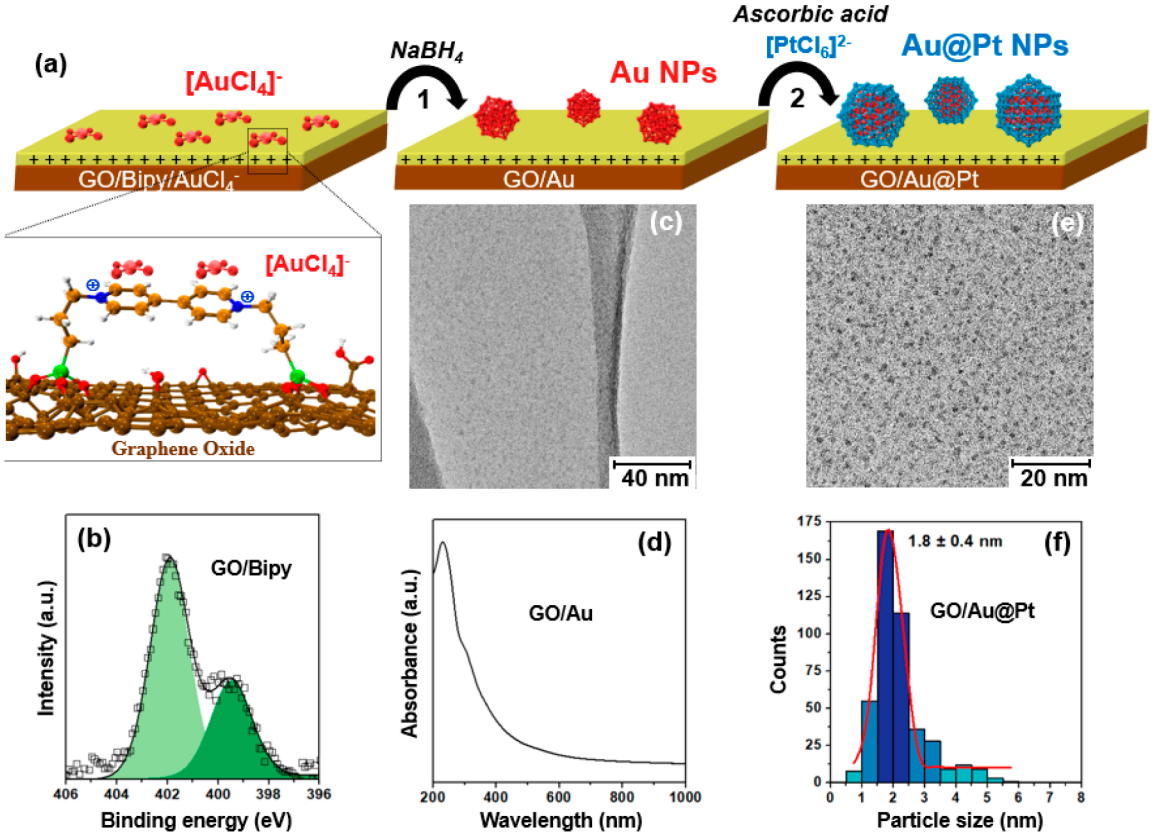

Figure 1. Schematic illustration of the (a) synthesis procedure of the ultrasmall bimetallic nanostructures (GO/Au@Pt) in the core−shell architecture and the cationic functional molecule covalently bonded to the surface of GO. (b) High-resolution (N 1s level) XPS spectrum of the functionalized GO/Bipy nanosheets. (c, d) TEM image and the UV−vis spectrum and of the GO/Au (seeds). (e, f) TEM image and the size-distribution histogram of the GO/Au@Pt nanostructures.

surface.[4] Considering these aspects, the ability to control the synthesis and the stabilization of ultrasmall bimetallic nanostructures and overcome the main drawbacks that were pointed out before is of paramount importance for the technological advances in the sustainable energy field.

Here, we demonstrate the synthesis of ultrasmall (<2 nm) Au@Pt core−shell nanostructures supported on functionalized graphene oxide (GO) nanosheets without the use of any passivating or capping agents. The developed synthetic route is based on the seed-mediated approach, starting from the in situ growth of the Au nanocrystals (core), followed by the heterogeneous nucleation of an ultrathin Pt shell. Density functional theory (DFT) calculations revealed significant differences on the electronic structure of the Au_{55}@Pt_{92} core−shell nanomaterial in comparison with Pt_{147} and $Au_{55}Pt_{92}$ (alloy) nanoparticles, highlighting a prominent increase on the density of states (DOS) near the Fermi level (E_F) for the Pt atoms on the shell (surface) for the Au_{55}@Pt_{92}. The electrocatalytic activities evaluated experimentally for the hydrogen evolution reaction (HER) corroborate with the calculated hydrogen adsorption Gibbs free energy (ΔG_H) and clearly reflects the observed alterations in the surface electronic states.

The first step in the synthesis of ultrasmall Au@Pt nanostructures involves the preparation of the Au core (seeds) by following a protocol reported for the synthesis of highly stable Au NPs supported on mesoporous silica.[14,15] As illustrated in Figure 1a, the anionic gold precursor ($AuCl_4^-$) is initially adsorbed on the surface of the GO nanosheets previously functionalized with cationic bipyridinium groups (Bipy), as confirmed by the X-ray photoelectron spectroscopy (XPS; N 1s) measurements (Figure 1b).[16] The ion-exchange properties of the functional molecules retain the $AuCl_4^-$ anions strongly attached on the surface by electrostatic interactions. The gold precursor is then converted into ultrasmall Au seeds by chemical reduction with $NaBH_4$.

Figure 1c shows a representative transmission electron microscopy (TEM) image of the GO/Au sample in which is possible to observe a low contrast of the metallic nanostructures supported on the GO nanosheets, evidencing their reduced sized. The absence of plasmonic bands in the visible range of the electromagnetic spectrum (Figure 1d) corroborates with the TEM observations and suggests that the Au seeds are small and homogeneous, with most of the particles at the size regime (<2 nm), where no surface plasmon resonance is observed.[17,18] The cationic bipyridinium groups, in combination with GO, may have an additional important role in stabilizing the Au seeds, thus avoiding uncontrolled growth and aggregation into larger nanoparticles.[14]

The growth of the Pt shell was subsequently carried out at room temperature by adding a plating solution containing the Pt precursor ($PtCl_6^{2-}$) and ascorbic acid (weak reducing agent) to the GO/Au (seeds) in aqueous suspension. Under these conditions, the reaction is expected to proceed via the controlled deposition of the Pt atoms on the surface of the preformed Au cores, and not by the undesired self-nucleation process of new Pt nuclei. The TEM images of the GO/Au@Pt can be seen in Figures 1e and S1, where the ultrasmall nature

DOI: 10.1021/acsami.8b12712
ACS Appl. Mater. Interfaces 2019, 11, 5661−5667

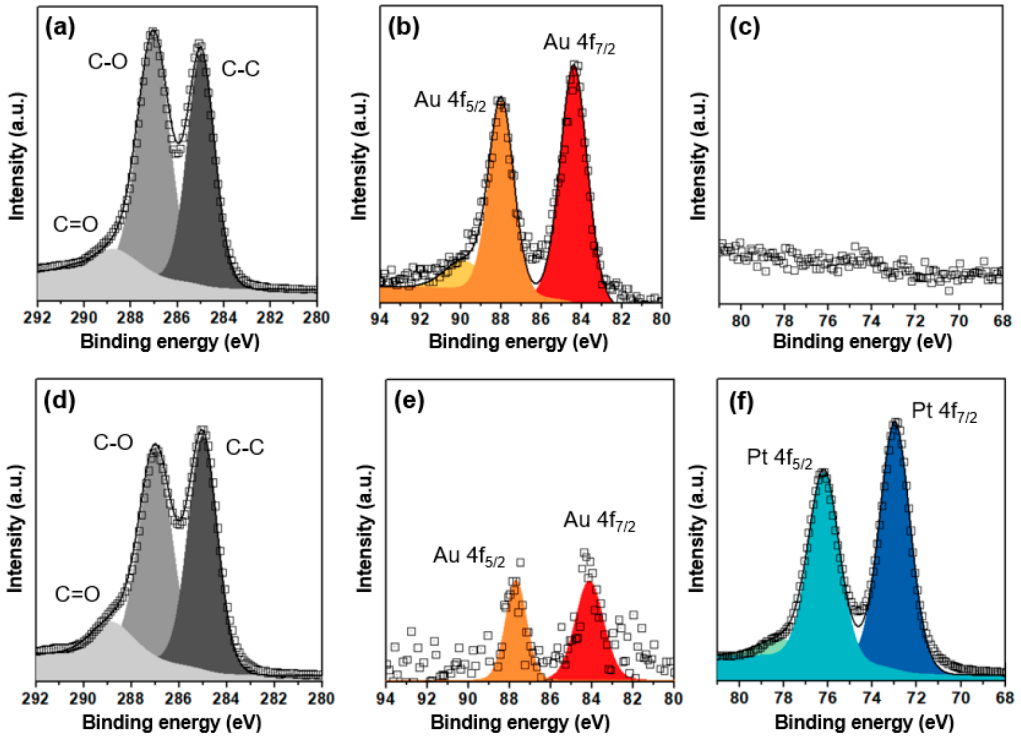

Figure 2. High-resolution XPS spectra of the (a–c) GO/Au and (d–f) GO/Au@Pt samples.

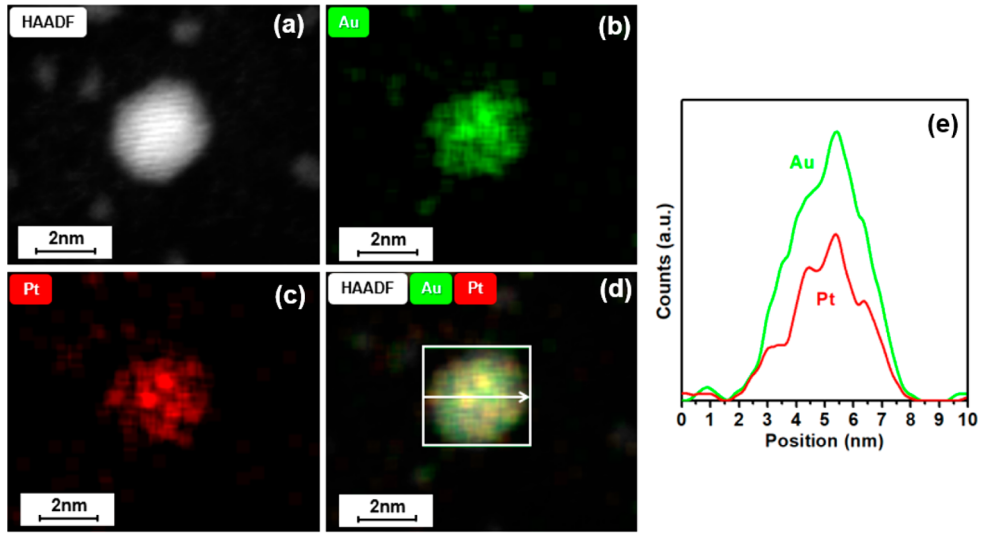

Figure 3. (a) HAADF-STEM image and the corresponding EDX mapping of (b) Au and (c) Pt for the Au@Pt sample. (d) The HAADF-STEM image with the EDX maps and (e) the line scan data.

of the metallic nanostructures is evident. The size histogram can be visualized in the Figure 1f. Scanning electron microscopy (SEM) images of GO/Au and GO/Au@Pt materials can also be seen in Figure S2. The resulting bimetallic system shows a narrow particle size distribution and high homogeneity, with an average size of ∼1.8 nm (ultrasmall regime), even without the use of stabilizing agents. Such reduced final size strongly suggests the obtaining of an atomically thin shell layer, thus maximizing the benefits from the electronic coupling and/or the strain effects imposed by the core on the outermost shell, which is extremely important for catalytic applications. As observed for the Au cores, the ultimate nanostructures are also highly stable on the surface of the functionalized GO, with no tendency for the formation of larger-sized nanostructures or aggregates.

High-resolution XPS spectra (Figures 2 and S3) of the GO/Au and GO/Au@Pt samples show the characteristic (C 1s) peaks of the graphene oxide, attributed to C−C, C−O, and C=O, and the Au 4f signals corresponding to the Au metallic cores (seeds).[19] After the growth of the Pt shell, a significant decrease in the intensity of the Au signal with respect to Pt is observed, which is consistent with the surface covering of the Au cores by the Pt layer. A small amount of metal oxide species (higher binding energy tails), usually observed on the XPS data of noble metal nanoparticles, is also detected on the GO/Au and GO/Au@Pt samples. The C 1s peaks of the GO/Au@Pt

DOI: 10.1021/acsami.8b12712
ACS Appl. Mater. Interfaces 2019, 11, 5661−5667

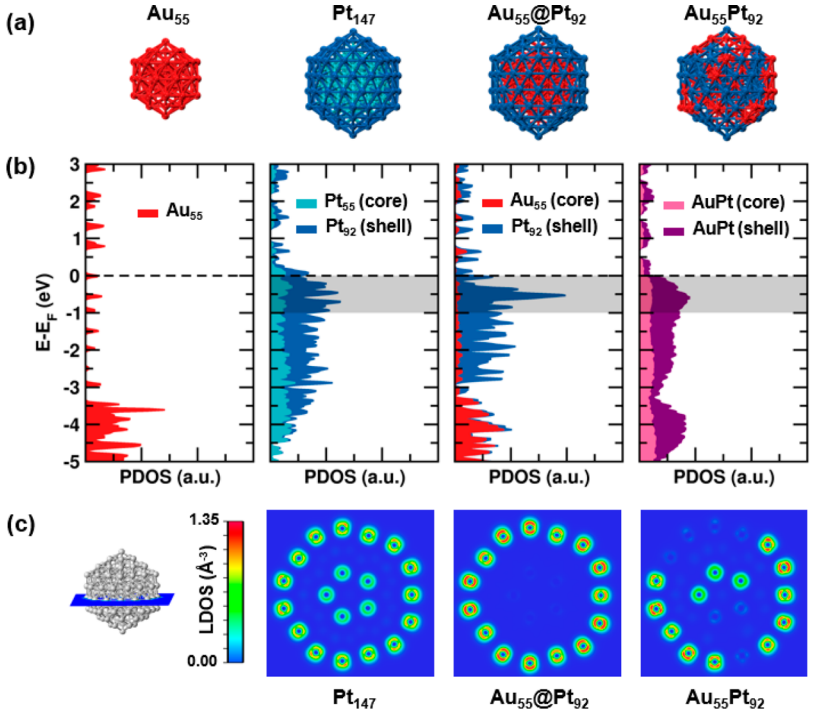

Figure 4. (a) Ball-and-stick model of ultrasmall Au_{55}, Pt_{147}, $Au_{55}@Pt_{92}$ (core−shell), and $Au_{55}Pt_{92}$ alloy nanostructures. (b) The respective projected density of states (PDOS). (c) Local density of states (LDOS) for low-energy quasiparticles for Pt_{147}, $Au_{55}@Pt_{92}$, and $Au_{55}Pt_{92}$ alloy across the plane shown in the left panel.

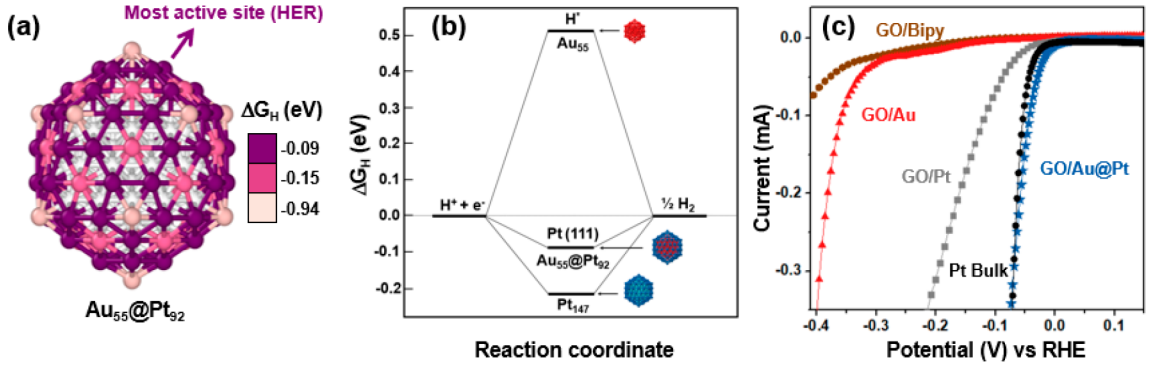

Figure 5. (a) Schematic illustration of three catalytic sites on the surface of the $Au_{55}@Pt_{92}$ nanostructure and the correspondent ΔG_H (hydrogen adsorption). (b) Free energy diagram of hydrogen evolution for the most active sites of Au_{55}, Pt_{147}, $Au_{55}@Pt_{92}$, and Pt (111). (c) HER polarization curves of GO/Bipy, GO/Au, GO/Pt, GO/Au@Pt, and Pt bulk electrodes carried out at 10 mV/s in 0.5 M H_2SO_4.

sample show minimal differences when compared to the GO/Au and indicate that the carbon support is slightly more reduced, probably due to the additional reduction step carried out to obtain the Au@Pt nanostructures.

Further evidence of the formation of the core−shell (Au@Pt) nanoparticles comes from the high-angle annular dark-field scanning transmission electron microscopy (HAADF-STEM) and the energy-dispersive X-ray spectrometry (EDX) (Figure 3). The HAADF-STEM image with the corresponding EDX data (maps and line scan) of Au and Pt of the metallic nanostructures clearly reveal that a thin Pt shell was successfully grown only on the surface of the Au seeds, forming the core−shell architecture. Neither segregated Pt clusters nor pure Pt nanoparticles were observed.

Metallic nanoparticles were modeled by first-principles methods based upon density functional theory. The structural and electronic properties were calculated for icosahedral nanoparticles:[20] (i) Au_{55} (1.20 nm), (ii) Pt_{147} (1.71 nm), (iii) $Au_{55}@Pt_{92}$ (1.74 nm), and (iv) $Au_{55}Pt_{92}$ randomly distributed alloy (1.74 nm). The icosahedral shape was chosen based on the formation energies of the Au core calculated for several geometries (Table S1). Figure 4a shows the ball-and-stick model for the optimized geometries of these metal nanostructures. The calculated projected densities of states (PDOS) for the four nanoparticles are shown in Figure 4b. For nanoparticles larger than 1.5 nm, the core and shell atoms were selected for electronic-state projections. Analyzing the electronic states near the Fermi level, we note that for Pt_{147} and $Au_{55}Pt_{92}$ alloy nanoparticles, there is a significant number of states located in the metal core. However, in the $Au_{55}@Pt_{92}$ core−shell configuration, a more-effective electronic transfer from gold to platinum is observed due to the differences in the work function of these metals. We can also note that there is a peak in the PDOS of the Pt shell around 0.5 eV below the

DOI: 10.1021/acsami.8b12712
ACS Appl. Mater. Interfaces 2019, 11, 5661−5667

Fermi level. For a more-detailed analysis of these states, we calculate the space-resolved local density of states (LDOS) for low-energy quasiparticles (-1 eV $< E - E_F < 0$). This energy range is shown as the shaded area (in gray) in Figure 3b.

In Figure 4c, we show the LDOS cross-section for Pt_{147}, $Au_{55}@Pt_{92}$, and $Au_{55}Pt_{92}$ alloy. For Pt_{147}, the low-energy quasiparticles are homogeneously distributed in all Pt atoms. Meanwhile, in the $Au_{55}@Pt_{92}$ nanoparticle, the low-energy quasiparticles are localized on the Pt shell. For comparison, we also calculated the LDOS for low-energy quasiparticles of the $Au_{55}Pt_{92}$ alloy, but these states are buried in the core. Other cross-sections are shown in Figure S4 in the LDOS tomography for low-energy quasiparticles. The high availability of electrons near the Fermi level can enhance surface phenomena, which are important, for instance, in heterogeneous catalysis and energy applications.

Considering these intensified surface electronic states, we calculate the quantitative descriptor for hydrogen evolution reaction (HER), given by the hydrogen adsorption Gibbs free energy (ΔG_H). From the Sabatier principle,[21] the catalytic activity is at its maximum at $\Delta G_H = 0$. This descriptor was calculated for various catalytic sites of the Au_{55}, Pt_{147}, and $Au_{55}@Pt_{92}$ nanostructures. Figure 5a shows the Gibbs free energy for three different Pt-sites on the $Au_{55}@Pt_{92}$ architecture. The most active site for HER refers to Pt atoms with the ΔG_H value closest to zero ($\Delta G_H = -0.09$ eV). The catalytic activity varies with the coordination number (C_N) of the Pt atoms. The Pt atoms with $C_N = 8$ shows the highest activity, followed by the Pt atoms with coordination number of 9 and 6. The Pt sites with $C_N = 8$ are the most frequent in the Pt shell, covering about 65% of the nanostructure surface. Besides these three sites, we calculate the catalytic activity for the hydrogen atoms bound to two metal atoms (bridge site) and three metal atoms (hollow site).[22] These sites and corresponding catalytic activity are shown in Table S2. Figure 5b shows the Gibbs free energy for the most active site for Au_{55}, Pt_{147}, and $Au_{55}@Pt_{92}$ nanostructures. For comparison purposes, the ΔG_H for the Pt(111) surface is also shown.[23] It is observed that the $Au_{55}@Pt_{92}$ and the Pt(111) are expected to have about the same catalytic activity and the highest among the evaluated materials. The most-active site for the Au_{55} (hollow site) has a very weak interaction with H* ($\Delta G_H = 0.52$ eV), while the most-active site for Pt_{147} (bridge site) has a very strong interaction ($\Delta G_H = -0.22$ eV) for HER. According to the ΔG_H values, it is expected the following trend in the catalytic activity: $Au_{55} < Pt_{147} < Pt(111) \cong Au_{55}@Pt_{147}$.

These observations were successfully confirmed by the experimental results, shown in Figures 5c and S5. The HER curves for the Pt (bulk) electrode and ITO substrates modified with thin films of GO/Bipy, GO/Au, GO/Pt, and GO/Au@Pt samples indicate exactly the same trend in terms of the catalytic activity as the one predicted by the first-principles calculations. The overpotential required for the hydrogen evolution reaction is much more favorable for the ultrasmall core–shell Au@Pt when compared to the monometallic Pt nanostructure.

In conclusion, we established an efficient route for the in situ synthesis of highly stable ultrasmall Au@Pt (~1.8 nm) nanostructures supported on functionalized graphene oxide nanosheets. Our route is highlighted by the absence of any passivation or capping agents. The DFT calculations of electronic properties show a charge transfer from the core (Au) to the surface atoms (Pt) in the core–shell $Au_{55}@Pt_{92}$ architecture, with a substantial increase of the surface electronic states when compared with equivalent Pt_{147} or $Au_{55}Pt_{92}$ alloy nanoparticles. The ΔG_H was also studied to have an in-depth understanding of the catalytic activity of the developed materials for HER. The predicted catalytic activity trend is consistent with the experimental results, highlighting the enhanced performance of the $Au_{55}@Pt_{92}$ nanomaterial. Finally, this work describes an attractive way for designing novel nanostructured metallic electrocatalysts by optimizing the active electronic states on the surface from both the experimental and the theoretical perspectives.

EXPERIMENTAL AND THEORETICAL METHODS

Synthesis and Functionalization of the Graphene Oxide Nanosheets. The synthesis and functionalization of the graphene oxide with the bipyridinium alkoxysilane (GO/Bipy) were carried out according to the procedure recently reported by our group.[24]

Synthesis of the GO/Au (Seeds). At first, 36 mL of the GO/Bipy was mixed with 360 μL of a $HAuCl_4$ aqueous solution (1% w/v). The mixture was kept under magnetic stirring for 4 h at room temperature and protected from light. The suspension was washed by centrifugation and resuspended in 36 mL of water. After that, the suspension was mixed with 3.2 mL of an iced cold aqueous solution of $NaBH_4$ (10 mmol/L) and stirred for 2 h. The final material was washed by centrifugation and resuspended in 36 mL in water (GO/Au). The same procedure was carried out for synthesis of Pt nanoparticles on the functionalized GO nanosheets (GO/Pt).

Synthesis of the GO/Au@Pt Core–shell Nanostructures. A total of 5 μL of H_2PtCl_6 (1% w/v) was added to 100 μL of GO/Au. The suspension was diluted with 375 μL of H_2O followed by the addition of 20 μL of 12.5 mmol/L fresh ascorbic acid aqueous solution. The mixture was vigorous stirred for 1 min. The reaction was aged for 2 h at room temperature, protected from light and without agitation. Finally, the washing step (centrifugation) was carried out to interrupt the reduction reaction. The resulting material (GO/Au@Pt) was resuspended in 500 μL of water.

Characterization. TEM measurements were performed in a JEOL JEM-2100 microscope operating at 200 kV. HAADF-STEM and EDX analysis were performed in Titan Themis Cubed FEI equipment with aberration correction operating at 300 kV. This microscope has a spectral resolution of 100 meV, lower than most electron microscopes, and guaranteed confidence in the identification of elements with very close energies such as Au (9.712 keV) and Pt (9.441 keV). The samples were deposited on lacey carbon TEM grids. X-ray photoelectron spectroscopy was performed on a Thermo Scientific Kα spectrometer. All spectra were taken using an Al Kα microfocused monochromatized source with a resolution of 0.100 eV, pass energy of 50 eV, and a spot size of 400 μm. The XPS data processing was carried out using the Thermo Scientific Avantage Software, including its peak deconvolution routines and the database of spectra to support the peak fitting. The peaks were fitted by using the Powell fitting algorithm and a Gaussian–Lorentzian product form function for all spectra. UV–vis spectroscopy was performed on a Thermo, Genesys 10S UV–vis Spectrophotometer. HER measurements were carried out using a Metrohm Autolab Potenciostat (model no. PGSTAT204) and a three-electrode cell configuration. Graphite rods and Ag/AgCl were used as auxiliary and reference electrodes. H_2SO_4 (0.5 mol/L) aqueous solution was used as the supporting electrolyte. The working electrodes were prepared by drop casting 1 μL of the aqueous suspensions of the samples (GO/Bipy, GO/Au, GO/Pt, and GO/Au@Pt) on indium–tin oxide (ITO) coated glass slides (2 cm × 0.5 cm). The electrochemical curves were obtained at a 10 mV/s scan rate.

DFT Calculations. The first-principles calculations based upon DFT[25,26] were performed as implemented in the SIESTA package.[27] We used the DZP localized basis, an energy shift of 0.03 eV, norm-conserved Troullier-Martins pseudopotentials,[28] and a mesh cutoff of 350 Ry. The exchange-correlation functional used was based on

DOI: 10.1021/acsami.8b12712
ACS Appl. Mater. Interfaces 2019, 11, 5661–5667

Perdew–Burke–Ernzerhof approximation.[29] All geometries were relaxed with maximal forces smaller than 0.030 eV/Å. The nanostructures were simulated in vacuum within a 27 nm^3 cubic cell. The electronic properties calculations were based on PDOS with Gaussian smearing of 0.04 eV and local density of states (LDOS) with an energy range of 1.0 eV below Fermi level. Data visualization of LDOS volume slices was performed with the VESTA program.[30]

The quantitative descriptor for HER was based on hydrogen adsorption Gibbs free energy, given by:

$$\Delta G_H = \Delta E_H + \Delta E_{ZPE} - T\Delta S_H$$

where:

$$\Delta E_H = E(M + H^*) - E(M) - \frac{1}{2}E(H_2)$$

is the semiclassical approximation for hydrogen adsorption energy on a material M. $E(M + H^*)$ is the total energy of the material M with a hydrogen adsorbed, $E(M)$ is the total energy of the material M when clean, and $E(H_2)$ is the total energy for a H_2 gas. ΔE_{ZPE} is the first-order quantum correction for the semiclassical approximation, the zero-point energy (ZPE) difference between adsorbed hydrogen (H^*) and H_2 gas. ΔS_H is the difference in entropy between adsorbed hydrogen and H_2 gas. Because the term $\Delta E_{ZPE} - T\Delta S_H$ relies weakly on the material M, we can use the Nørskov approximation:[23]

$$\Delta G_H = \Delta E_H + 0.24\text{eV}$$

■ ASSOCIATED CONTENT

Supporting Information

The Supporting Information is available free of charge on the ACS Publications website at DOI: 10.1021/acsami.8b12712.

SEM and TEM images of the GO/Au and GO/Au@Pt samples; XPS spectra of GO/Au and GO/Au@Pt samples, tomography of local density of states (LDOS) for low-energy quasiparticles for Pt_{147}, Au_{55}@Pt_{92} and $Au_{55}Pt_{92}$ alloy nanoparticles, the formation energy for several shapes of the Au core and the Au@Pt nanoparticles, and Gibbs free energy values for the hydrogen adsorption at different sites and Tafel plots for HER (PDF)

■ AUTHOR INFORMATION

Corresponding Authors

*E-mail: leandro.seixas@mackenzie.br.
*E-mail: camila.maroneze@mackenzie.br.

ORCID

Valeria S. Marangoni: 0000-0002-3732-504X
Leandro Seixas: 0000-0001-7420-0708
Camila M. Maroneze: 0000-0002-6835-4476

Notes

The authors declare no competing financial interest.

■ ACKNOWLEDGMENTS

The authors acknowledge the financial support from FAPESP (grant nos. 2012/50259-8, 2016/20799-1, and 2017/00486-1) and CNPq (grant nos. 432544/2016-0 and 306422/2017-4). We also acknowledge CNPEM-LNNano for the technical support during TEM and XPS measurements (TEM-21323 and XPS-21327), and Centre for Advanced 2D Materials, National University of Singapore for high-performance computational facilities.

■ REFERENCES

(1) Liu, L.; Corma, A. Metal Catalysts for Heterogeneous Catalysis: From Single Atoms to Nanoclusters and Nanoparticles. *Chem. Rev.* **2018**, *118* (10), 4981–5079.
(2) Jin, H.; Guo, C.; Liu, X.; Liu, J.; Vasileff, A.; Jiao, Y.; Zheng, Y.; Qiao, S. Z. Emerging Two-Dimensional Nanomaterials for Electrocatalysis. *Chem. Rev.* **2018**, *118* (13), 6337–6408.
(3) Voiry, D.; Shin, H. S.; Loh, K. P.; Chhowalla, M. Low-Dimensional Catalysts for Hydrogen Evolution and CO2 Reduction. *Nat. Rev. Chem.* **2018**, *2* (1), 0105.
(4) Gilroy, K. D.; Ruditskiy, A.; Peng, H. C.; Qin, D.; Xia, Y. Bimetallic Nanocrystals: Syntheses, Properties, and Applications. *Chem. Rev.* **2016**, *116* (18), 10414–10472.
(5) Laskar, M.; Skrabalak, S. E. A Balancing Act: Manipulating Reactivity of Shape-Controlled Metal Nanocatalysts through Bimetallic Architecture. *J. Mater. Chem. A* **2016**, *4* (18), 6911–6918.
(6) Ghosh Chaudhuri, R.; Paria, S. Core/Shell Nanoparticles: Classes, Properties, Synthesis Mechanisms, Characterization, and Applications. *Chem. Rev.* **2012**, *112* (4), 2373–2433.
(7) Bligaard, T.; Nørskov, J. K. Ligand Effects in Heterogeneous Catalysis and Electrochemistry. *Electrochim. Acta* **2007**, *52* (18), 5512–5516.
(8) Tedsree, K.; Li, T.; Jones, S.; Chan, C. W. A.; Yu, K. M. K.; Bagot, P. A. J.; Marquis, E. A.; Smith, G. D. W.; Tsang, S. C. E. Hydrogen Production from Formic Acid Decomposition at Room Temperature Using a Ag–Pd Core–shell Nanocatalyst. *Nat. Nanotechnol.* **2011**, *6* (5), 302–307.
(9) Stamenkovic, V.; Mun, B. S.; Mayrhofer, K. J. J.; Ross, P. N.; Markovic, N. M.; Rossmeisl, J.; Greeley, J.; Nørskov, J. K. Changing the Activity of Electrocatalysts for Oxygen Reduction by Tuning the Surface Electronic Structure. *Angew. Chem., Int. Ed.* **2006**, *45* (18), 2897–2901.
(10) Kibler, L. A.; El-Aziz, A. M.; Hoyer, R.; Kolb, D. M. Tuning Reaction Rates by Lateral Strain in a Palladium Monolayer. *Angew. Chem., Int. Ed.* **2005**, *44* (14), 2080–2084.
(11) Jana, N. R.; Gearheart, L.; Murphy, C. J. Wet Chemical Synthesis of Silver Nanorods and Nanowires of Controllable Aspect Ratio. *Chem. Commun.* **2001**, *7*, 617–618.
(12) Ghosh Chaudhuri, R.; Paria, S. Core/Shell Nanoparticles: Classes, Properties, Synthesis Mechanisms, Characterization, and Applications. *Chem. Rev.* **2012**, *112* (4), 2373–2433.
(13) Kim, B. H.; Hackett, M. J.; Park, J.; Hyeon, T. Synthesis, Characterization, and Application of Ultrasmall Nanoparticles. *Chem. Mater.* **2014**, *26* (1), 59–71.
(14) Fattori, N.; Maroneze, C. M.; Da Costa, L. P.; Strauss, M.; Sigoli, F. A.; Mazali, I. O.; Gushikem, Y. Ion-Exchange Properties of Imidazolium-Grafted SBA-15 toward AuCl 4- Anions and Their Conversion into Supported Gold Nanoparticles. *Langmuir* **2012**, *28* (27), 10281–10288.
(15) Fattori, N.; Maroneze, C. M.; Costa, L. P. D.; Strauss, M.; Mazali, I. O.; Gushikem, Y. Chemical and Photochemical Formation of Gold Nanoparticles Supported on Viologen-Functionalized SBA-15. *Colloids Surf., A* **2013**, *437*, 120–126.
(16) Alvaro, M.; García, H.; García, S.; Márquez, F.; Scaiano, J. C. Intrazeolite Photochemistry. 17. Zeolites as Electron Donors: Photolysis of Methylviologen Incorporated within Zeolites. *J. Phys. Chem. B* **1997**, *101* (16), 3043–3051.
(17) Kim, Y.-G.; Oh, S.-K.; Crooks, R. M. Preparation and Characterization of 1–2 Nm Dendrimer-Encapsulated Gold Nanoparticles Having Very Narrow Size Distributions. *Chem. Mater.* **2004**, *16* (1), 167–172.
(18) Young, J. K.; Lewinski, N. A.; Langsner, R. J.; Kennedy, L. C.; Satyanarayan, A.; Nammalvar, V.; Lin, A. Y.; Drezek, R. A. Size-Controlled Synthesis of Monodispersed Gold Nanoparticles via Carbon Monoxide Gas Reduction. *Nanoscale Res. Lett.* **2011**, *6*, 428.
(19) Ruzicka, J. Y.; Abu Bakar, F.; Hoeck, C.; Adnan, R.; Mcnicoll, C.; Kemmitt, T.; Cowie, B. C.; Metha, G. F.; Andersson, G. G.; Golovko, V. B. Toward Control of Gold Cluster Aggregation on TiO2

DOI: 10.1021/acsami.8b12712
ACS Appl. Mater. Interfaces 2019, 11, 5661–5667

via Surface Treatments. *J. Phys. Chem. C* **2015**, *119* (43), 24465−24474.
(20) Barnard, A. S.; Young, N. P.; Kirkland, A. I.; Van Huis, M. A.; Xu, H. Nanogold: A Quantitative Phase Map. *ACS Nano* **2009**, *3* (6), 1431−1436.
(21) Norskov, J. K.; Studt, F.; Abild-Pedersen, F.; Bligaard, T. *Fundamental Concepts in Heterogenous Catalysis*; Wiley, Ed.; John Wiley & Sons, Inc.: Hoboken, NJ, 2014.
(22) Tan, T. L.; Wang, L. L.; Zhang, J.; Johnson, D. D.; Bai, K. Platinum Nanoparticle during Electrochemical Hydrogen Evolution: Adsorbate Distribution, Active Reaction Species, and Size Effect. *ACS Catal.* **2015**, *5* (4), 2376−2383.
(23) Nørskov, J. K.; Bligaard, T.; Logadottir, A.; Kitchin, J. R.; Chen, J. G.; Pandelov, S.; Stimming, U. Trends in the Exchange Current for Hydrogen Evolution. *J. Electrochem. Soc.* **2005**, *152* (3), J23.
(24) Marangoni, V. S.; Germano, L. D.; Silva, C. C. C.; de Souza, E. A.; Maroneze, C. M. Engineering Two-Dimensional Gold Nanostructures Using Graphene Oxide Nanosheets as a Template. *Nanoscale* **2018**, *10* (28), 13315−13319.
(25) Hohenberg, P.; Kohn, W. The Inhomogeneous Electron Gas. *Phys. Rev.* **1964**, *136* (3B), B864.
(26) Kohn, W.; Sham, L. J. Self-Consistent Equations Including Exchange and Correlation Effects. *Phys. Rev.* **1965**, *140* (4A), 1133.
(27) Soler, J. M.; Artacho, E.; Gale, J. D.; García, A.; Junquera, J.; Ordejón, P.; Sánchez-Portal, D. The SIESTA Method for Ab Initio Order-N Materials Simulation. *J. Phys.: Condens. Matter* **2002**, *14* (11), 2745−2779.
(28) Troullier, N.; Martins, J. L. Efficient Pseudopotentials for Plane-Wave Calculations. II. Operators for Fast Iterative Diagonalization. *Phys. Rev. B: Condens. Matter Mater. Phys.* **1991**, *43* (11), 8861−8869.
(29) Perdew, J. P.; Burke, K.; Ernzerhof, M. Generalized Gradient Approximation Made Simple. *Phys. Rev. Lett.* **1996**, *77* (18), 3865−3868.
(30) Momma, K.; Izumi, F. VESTA for Three-Dimensional Visualization of Crystal, Volumetric and Morphology Data. *J. Appl. Crystallogr.* **2011**, *44* (6), 1272−1276.

DOI: 10.1021/acsami.8b12712
ACS Appl. Mater. Interfaces 2019, 11, 5661−5667